Powder Technology 412 (2022) 117996

Contents lists available at ScienceDirect

Powder Technology

journal homepage: www.journals.elsevier.com/powder-technology

Factors determining the flowability and spreading quality of gas-atomized Ti-48Al-2Cr-2Nb powders in powder bed fusion additive manufacturing

Seungkyun Yim *, Kenta Aoyagi *, Huakang Bian, Yujie Cui, Akihiko Chiba

Institute for Materials Research, Tohoku University, 2-1-1 Katahira, Sendai, Miyagi 980-8577, Japan

HIGHLIGHTS

- Flowability of GA powder under the dynamic condition was improved after ball milling owing to the decreased cohesion force.
- High cohesive force in GA powder was mainly attributed to the electrostatic force caused by charge accumulation on the oxide film.
- Spreadability of GA powder was improved after ball milling due to the decreased cohesion force.

GRAPHICAL ABSTRACT

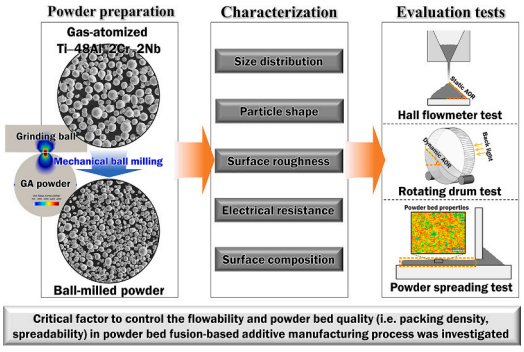

ARTICLE INFO

Keywords:
Powder bed fusion additive manufacturing
Powder spreading
Flowability
Cohesion force
Spreadability
Electrostatic force

ABSTRACT

A high-quality powder bed is necessary for obtaining high-quality products using powder bed fusion-based additive manufacturing. In this study, mechanical ball milling was suggested to improve the flowability and spreadability of gas-atomized (GA) Ti–48Al–2Cr–2Nb powder in the powder bed fusion additive manufacturing process. The deformation mechanism of the GA powder significantly differed depending on the ball milling media. Surface grinding mainly occurred during Al_2O_3 ball milling, while the pulverization was dominant in WC ball milling because of the higher impact force. The flowability of the GA powder under dynamic conditions was improved after Al_2O_3 and WC ball milling owing to the decreased cohesive force. The high cohesive force in the GA powder under dynamic conditions was attributed to the electrostatic force caused by charge accumulation on the oxide film. The packing density of GA powder was increased after WC ball milling despite the formation of numerous irregular particles owing to the synergetic effect of rapid energy dissipation, minimized wall effect, and void filling effect. Furthermore, the spreadability of the GA powder was improved by ball milling because of the decrease in the cohesive force. Therefore, it was demonstrated that the flowability and spreadability of the GA powder can be improved via ball milling because of changes in particle size, shape, and surface properties.

* Corresponding authors.
E-mail addresses: yim.seungkyun.a3@tohoku.ac.jp (S. Yim), kenta.aoyagi.e7@tohoku.ac.jp (K. Aoyagi).

https://doi.org/10.1016/j.powtec.2022.117996
Received 9 August 2022; Received in revised form 30 September 2022; Accepted 5 October 2022
Available online 12 October 2022

1. Introduction

In the last decade, powder bed fusion additive manufacturing (PBF-AM) techniques have attracted significant attention in the industrial fields because they enable rapid prototyping, near-net-shape design, and short process lead time [1]. For instance, General Electric and Rolls Royce fabricated some parts for aircraft and automotive industries using the PBF-AM to improve fuel efficiency using the structural design [2–4]. The powder feedstock in the PBF-AM process is dropped from the feedstock chamber and spread by a stainless-steel blade or rotating roller on the building stage [5]. The deposited thin powder layer is then selectively melted using the high-energy heat source based on the sliced computer-aided design data. The powder spreading and selective melting processes are repeated layer by layer until the completion of the three-dimensional product. Several studies reported the significance of high-quality powder beds in PBF-AM. Boley et al. reported that laser absorption in powder bed was substantially affected by particle size distribution (PSD) in laser powder bed fusion (L-PBF) [6]. Lee et al. reported low melt pool stability at a low-quality powder bed, resulting in balling defects during L-PBF [7]. Zhao et al. pointed out that the heat absorption and conduction, which determine the molten pool and solidification behaviors, were significantly affected by powder bed properties in the powder bed fusion electron beam (PBF-EB) process [8–10]. Rausch et al. reported that the high packing density of powder bed can significantly reduce the internal defects of the product in the PBF-EB process [11]. Therefore, the high-quality powder bed is a prerequisite to obtaining high-quality products without defects in the PBF-AM process.

The powder bed quality is significantly affected by powder properties and process parameters in the powder spreading process [12]. The powder bed quality has been improved by optimizing the spreading process parameters such as spreading velocity, layer thickness, spreader geometry, and vibration method [13–16], but there is still controversy regarding the major factors affecting the powder bed quality in the powder spreading process. Snow et al. reported that the increase in the angle of repose worsened powder spreading quality, and the spreadability was mainly controlled by powder characteristics rather than spreading parameters [17]. Mussatto et al. confirmed that the quality of powder bed could not be explained by flowability alone—it was mainly affected by the spherical shape and surface smoothness of the powder [18]. Yim et al. demonstrated using coupled experimental and discrete element method simulation studies that the packing density of the powder bed was predominantly affected by PSD rather than particle shape or surface properties [19]. Chen et al. pointed out that the powder bed quality is mainly controlled by the PSD, and that the presence of fine particles smaller than 21.8 μm results in low packing density owing to the increased cohesive force [20]. Thus, the major factor among the powder properties controlling the powder bed quality should be clarified to improve powder bed quality in the PBF-AM process. Furthermore, several studies suggested pretreatment for the powder to improve the product quality produced via the PBF-AM process using surface coating, sputtering, and chemical treatments, but these methods were limited owing to the process difficulty and high cost [21–23]. Thus, cost-effective pretreatment to improve the spreadability and packing density of the powder bed in the PBF-AM process should be suggested.

In the previous study, we reported that the electrical properties of Inconel 718 and Ti–48Al–2Cr–2Nb powders, containing 3d transition metal oxides, can be transitioned from insulating to metallic via mechanical stimulation using ball milling [24–26]. Furthermore, the ball-milled Inconel 718 and Ti–48Al–2Cr–2Nb powders were heated by electron beam irradiation in the PBF-EB process without smoke generation even at room temperature. However, ball milling results in variation in particle size and shape depending on the milling conditions and grinding media. Therefore, the effect of ball milling on the flowability of powder and powder bed quality should be investigated.

In this study, ball milling was used to improve the flowability and spreadability of gas-atomized (GA) Ti–48Al–2Cr–2Nb alloy in the PBF-AM process. The two types of ball milling media were tested to control the particle size, shape, and surface properties of the virgin powder. The flowability of the powder was evaluated under gravitational and rotating conditions using the Hall flowmeter and rotating drum tests, respectively. The powder bed properties were examined using specially designed spreading equipment under various spreading speeds and layer thicknesses. Finally, the factor determining the flowability and powder bed quality was determined based on the particle properties. We believe that this study contributes to improving the understanding of the powder spreading mechanism and improvement of the powder bed quality in the PBF-AM process.

Table 1
Oxygen concentrations in the GA and ball-milled Ti–48Al–2Cr–2Nb powders.

Sample	GA	BM-A	BM-W
O concentration (wt%)	0.0657	0.0691	0.067

2. Materials and methods

2.1. Mechanical ball milling

The virgin Ti–48Al–2Cr–2Nb (at.%) powder produced by gas atomization was provided by Daido steel Co., LTD., Japan. Its specific chemical composition and microstructure can be found in our previous study [24]. The virgin powder was ball milled to manipulate its particle size, shape, and surface properties. The Al_2O_3 and WC milling vials and grinding balls (prepared by Fritsch GmbH, Germany) were used in this study. The 33 vol% of Al_2O_3 (5 mm in diameter) and WC (6 mm in diameter) grinding balls were placed in the milling vials, followed by the addition of the 33 vol% of the GA powder. All these operations were performed in the glove box under Ar atmosphere. Ball milling was performed at 400 rpm for 40 min using a planetary high-energy ball mill (Pulverisette 7, Fritsch GmbH, Germany). The Ar gas was recharged into milling vials at intervals of 20 min using the glove box system to ensure milling under inert atmosphere. For convenience, the powders ball-milled using Al_2O_3 and WC grinding media are referred to as BM-A and BM-W, respectively. The oxygen contamination owing to ball milling was examined using an oxygen–nitrogen analyzer (ON736, Leco Corp., Japan). The results confirmed that the oxygen contamination of the GA powder did not occur during ball milling under Ar atmosphere, as shown in Table 1.

2.2. Particle size and shape analysis

The particle morphology was observed using scanning electron microscopy (SEM, S-3400 N, Hitachi High-Tech Science Corp., Japan). The PSDs of the GA and ball-milled powders were determined via the linear intercept method following ASTM-E112 using >1000 particles. The particle morphology distribution (PMD) map was developed to characterize the particle shape evolution via ball milling. The particle pixel data from the SEM images was computed via the thresholding contrast method using the ImageJ software (National Institutes of Health, USA) [27]. The roundness (ϕ_R) and sphericity (ψ_S) of particles were computed as follows:

$$\phi_R = \frac{r_a}{r_p} \tag{1}$$

$$\psi_S = \frac{r_a}{r_m} \tag{2}$$

where the r_a, r_p, and r_m are the particle radii calculated using the area, perimeter, and major axis from the binary images, respectively. In the PMD map, the low sphericity indicates the elongated particle shape, and the low roundness indicates the irregularity of particle shape. The values

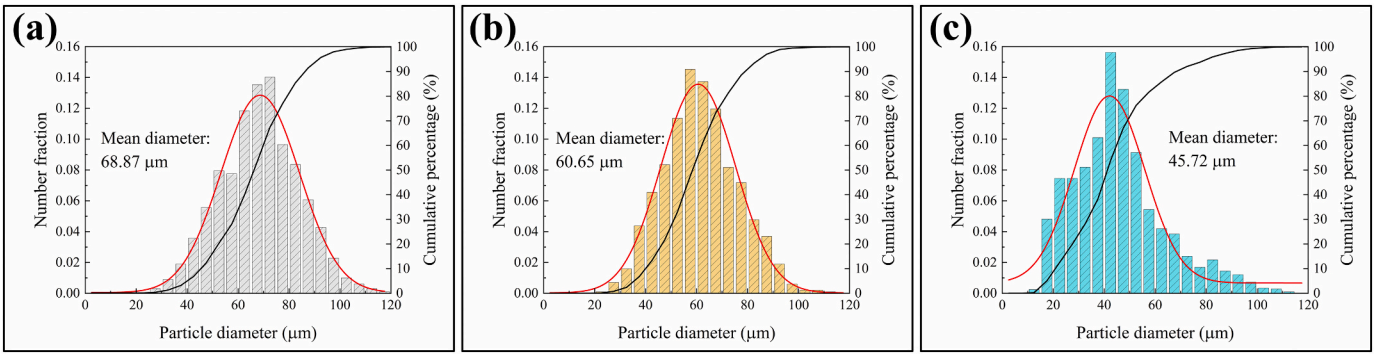

Fig. 1. Particle size distribution of Ti–48Al–2Cr–2Nb powders: (a) GA, (b) BM-A, (c) BM-W.

of sphericity and roundness were obtained with an interval of 0.1, and the fraction of elongated particles was determined to total fraction of $\psi_S < 0.9$. The multivariate kernel density estimation was employed to visualize overlapping data points in the PMD map according to the following equation:

$$f(x,y) = \frac{1}{n}\sum_{i=1}^{n}\frac{1}{2\pi w_x w_y} exp\left(-\frac{(x-vX_i)^2}{2w_x^2} - \frac{(y-vY_i)^2}{2w_y^2}\right) \quad (3)$$

where f is the kernel density estimate, n is the number of elements in vector vX or vY, subscript i is the ith element in the vector, and w_x and w_y are the optimal bandwidths values, respectively. To characterize the surface-attached satellites in particles, the fraction of satellite-contained particles was carefully measured by counting the number of particles with surface-attached satellites on >1000 particles.

2.3. Flowability and powder spreading test

The gravity-based flowability of the powders was examined using a Hall flowmeter (JIS-Z2502, Tsutsui Scientific Instruments Co., Ltd., Japan) based on the ASTM B213 standard. The static angle of repose (AOR) was determined to be the average slope angle of the deposited powder dummy without collapse using the edge tracing linear regression method. The rotation-induced flowability of the powders was examined using the rotating drum test at an angular velocity of 10 rpm. The dynamic AOR was determined to be an average angle of the upper avalanche slope in the constant flow regime. The detailed flowability test methods can be found in the previous study [19]. The powder spreading test was conducted to evaluate the packing density and surface roughness of powder beds using specially designed powder spreading equipment. The powder (50 g) was poured on the base plate and then spread with a blade at the velocities of 50, 150, and 250 mm/s. The layer thickness during powder spreading ranged from 100 to 200 μm, which is a range of effective layer thickness in the PBF-AM process [28]. The surface roughness of the powder bed (ξ_{SR}) was evaluated using the 3D optical profilometer (VR-3200, Keyence Corp., Japan) with a resolution of ±2.5 μm as follows:

$$\xi_{SR} = \frac{1}{A}\iint_A |Z(x,y)|dxdy \quad (4)$$

where A is the total sampling dimension, and Z is the height variation in the profile point. The packing density of the spread powder bed was

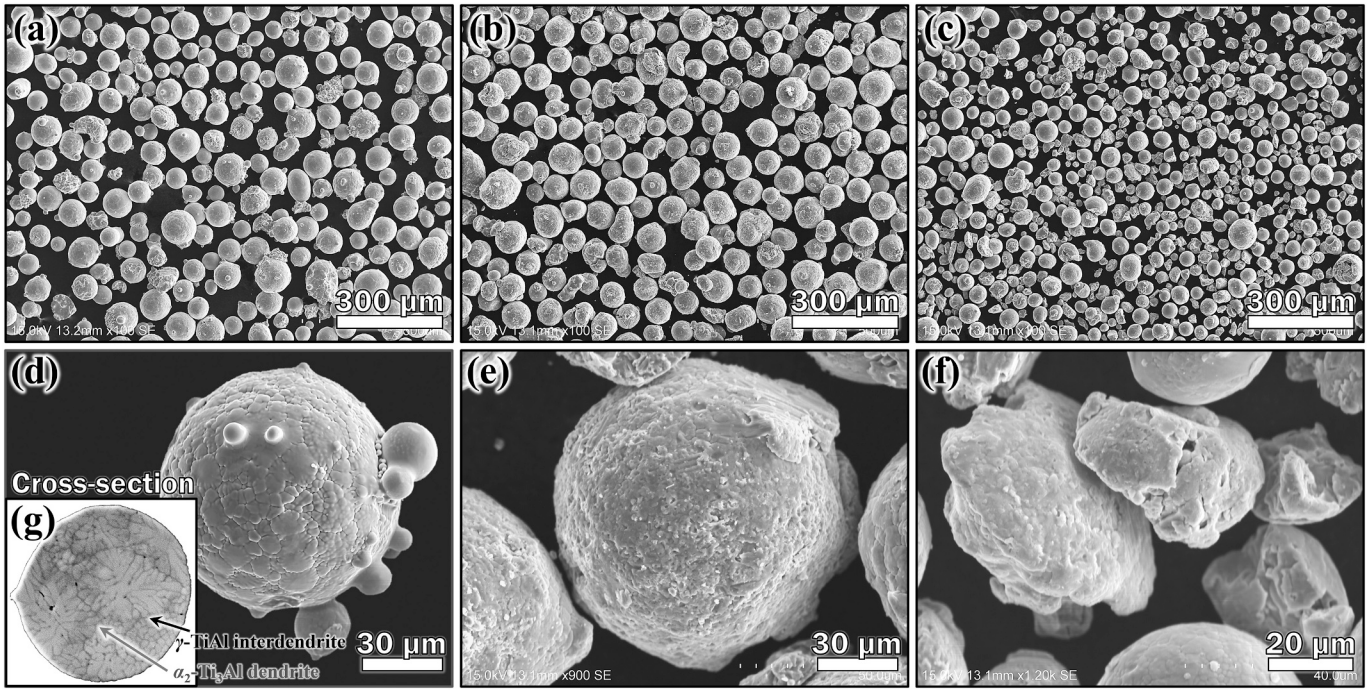

Fig. 2. Surface morphology images of Ti–48Al–2Cr–2Nb powders: (a), (d) GA, (b), (e) BM-A, and (c), (f) BM-W. (g) Cross-sectional BSE image of GA Ti–48Al–2Cr–2Nb powder.

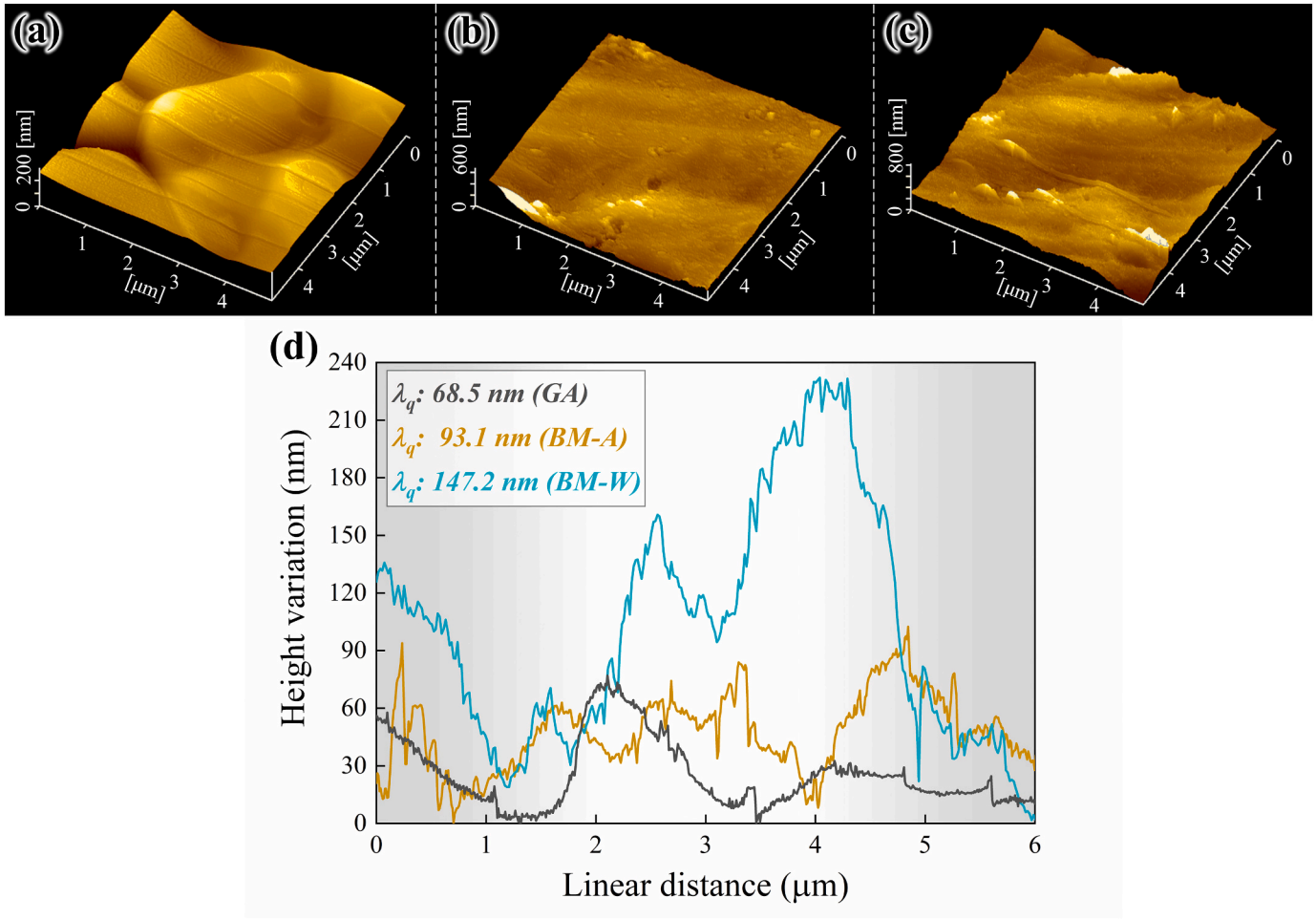

Fig. 3. Nanoscale surface topography of Ti–48Al–2Cr–2Nb powders: (a) GA, (b) BM-A, and (c) BM-W. (d) Height variation in the GA and ball-milled powders. (λ_q indicates average roughness).

calculated using gain powder mass according to the following equation:

$$\rho_{PB} = \frac{m}{V_{PB}} \times \frac{100}{\rho_t} \tag{5}$$

where V_{PB} is the theoretical volume of the spreading area, m is the weight of the deposited powder bed, and ρ_t is the true density of the Ti–48Al–2Cr–2Nb alloy (3.87 g/cm^3). The powder spreading test was performed five times to obtain packing density deviation owing to the discrete nature of the powder.

2.4. Analysis of surface and electrical properties

The chemical compositions of the GA and ball-milled powders were examined using X-ray photoelectron spectroscopy (XPS, PHI5000 VersaProbe II, ULVAC-PHI Inc., Japan) with a monochromatic Al Kα source (1486.7 eV) in a survey scan mode. The chemical compositions were further characterized by high-resolution narrow-scan profiles near the O *1 s*, Ti *2p*, Al *2p*, Cr *2p*, and Nb *3d* element peaks. The XPS spectra were analyzed using COMPRO software package with the Shirley background.

The direct current (DC) resistivity and alternating current (AC) impedance spectroscopy tests were conducted using a tailored contact device in a vacuum environment. A four-point probe measurement was performed to evaluate the DC electrical resistivity of the powders. The powder (2.45 g) was placed inside the Al_2O_3 cylinder, which was further sealed with a Pt plate. Both sides of the powder sample were compressed by the electrode with 10 N to maintain constant contact between the particles. The AC impedance spectroscopy was performed to characterize the equivalent electrical circuit of powders. The impedance of the powders was determined in the frequency range of 1 Hz–5 × 10^6 Hz using an LCR meter (ZM 2376 LCR, NF Corp., Japan) to characterize the inductance (L), capacitance (C), and resistance (R) of an electrical circuit component. The impedance data was analyzed using the EC-LAB software package (BioLogic Science Instruments Ltd., France) to determine the possible electrical circuit and charge dissipation time of the capacitor. Further details on the impedance analysis can be found in the previous study [24–26].

3. Results and discussion

3.1. Effect of ball milling on PSD and morphology

The PSDs of the GA and ball-milled powders are presented in Fig. 1a–c. The particle size of the GA powder ranges from 25 to 120 μm, and its mean diameter is 68.87 μm. The peak position in PSD of the GA powder is slightly shifted to the left side after ball milling using the Al_2O_3 media, while it is significantly shifted after ball milling using the WC media. The mean particle diameter of GA powder was slightly decreased to 60.65 μm after Al_2O_3 ball milling, while it was far decreased to 45.72 μm after WC ball milling.

The surface images of the GA and ball-milled powders are presented in Fig. 2a–f. The GA powder is composed of spherical and elongated particles with several satellites and coarse flexural texture on the surface (Fig. 2a and d). The dendritic microstructure consisting of α_2-Ti_3Al and γ-TiAl phases is observed in the cross-sectional basckscattered electron

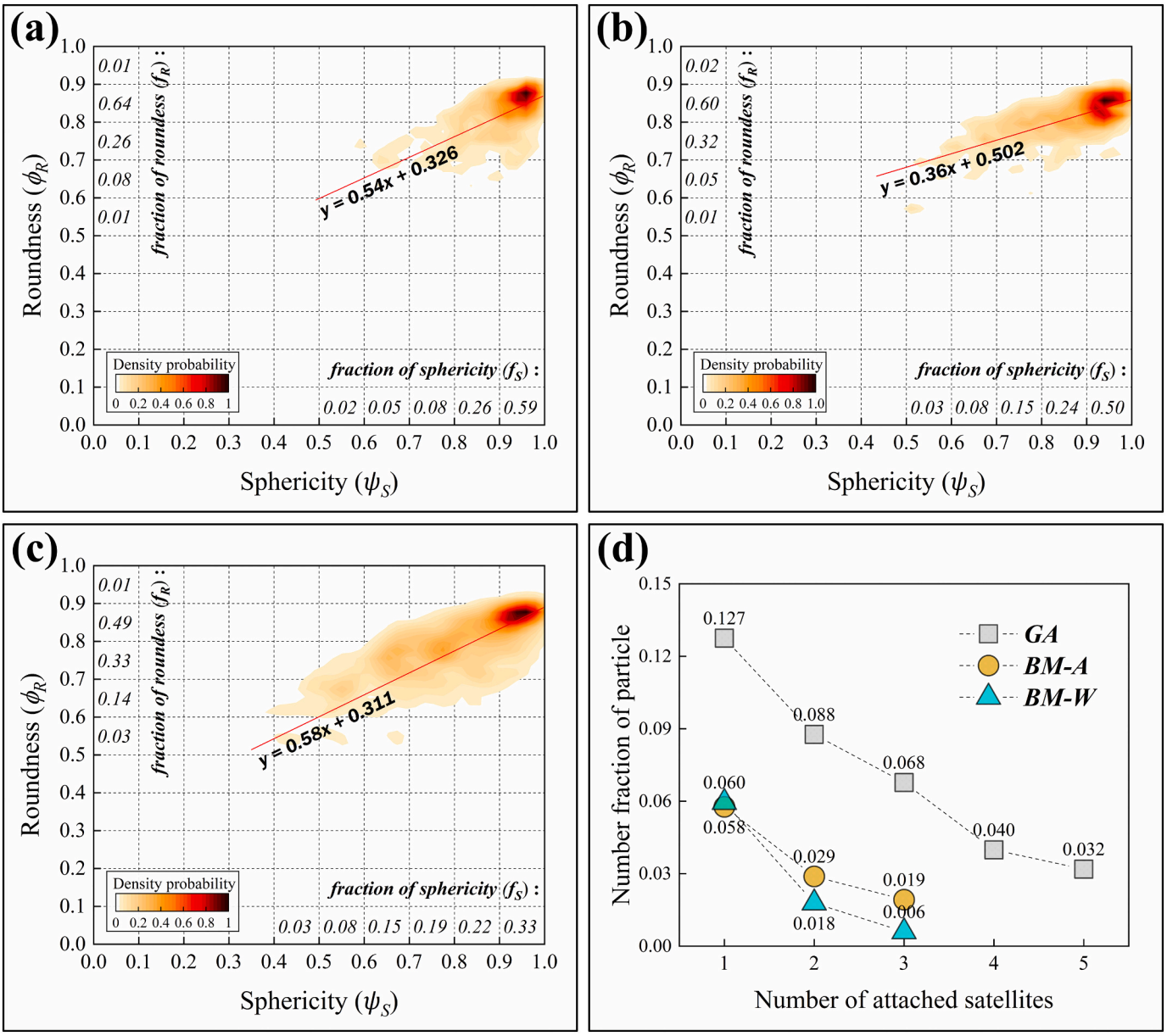

Fig. 4. Particle morphology distribution of Ti–48Al–2Cr–2Nb powders: (a) GA, (b) BM-A, and (c) BM-W. (d) Fractions of satellite-containing particles in the GA and ball-milled powders.

(BSE) image of the GA powder (Fig. 2g). This result suggests that the coarse flexural surface of the GA powder could be attributed to the dendritic solidification caused by rapid cooling during gas atomization [29]. In the BM-A powder, the particles are spherical and elongated without satellites, and the surface is deformed rather than coarse flexural because of ball milling (Fig. 2b and e). The BM-W powder contains spherical and flake-shaped particles, and the fractured surface of flake particles has irregular morphology at a microscale (Fig. 2c and f). This result suggests that the deformation behavior of the GA powder during ball milling strongly depends on the ball milling media.

The nanoscale surface morphology and height variation in the GA and ball-milled powders are presented in Fig. 3a–d. The GA particle shows a fluctuating dendritic surface with a surface roughness (λ_q) of 68.5 nm (Fig. 3a). The λ_q of the GA powder increased after ball milling with Al_2O_3 (93.1 nm) despite the removal of the flexural texture; at the same time, after ball milling with WC, λ_q significantly increased (147.2 nm), as shown in Fig. 3b–d. This result indicates that the mechanical deformation via ball milling could locally occur on the particle surface, and the accumulated deformations could result in variations in surface height at a nanoscale.

The PMD and the fraction of satellite-contained particles in the GA and ball-milled powders are shown in Fig. 4a–d. In the PMD map, the surface irregularity trend of the powder can be represented using the shape factor (k) obtained via linear regression: $y = kx + b$ [26]. The fraction of elongated particles is 0.41 for the GA powder, and the shape factor is 0.54. The fraction of elongated particles increased to 0.5 in the BM-A powder, while the shape factor decreased to 0.36, indicating a smoother surface than in the GA powder. The fraction of elongated particles is significantly increased to 0.67 in the BM-W powder, and its shape factor is 0.58, indicating a more irregular particle surface than in the GA powder. The fraction of satellite-containing particles in the GA powder is 0.355, and it is significantly decreased to 0.106 and 0.084 after ball milling with Al_2O_3 and WC, respectively. This result indicates that the decrease in shape factor after ball milling with Al_2O_3 could be attributed to the removal of surface-attached satellites, while the increase in shape factor after ball milling with WC could be attributed to

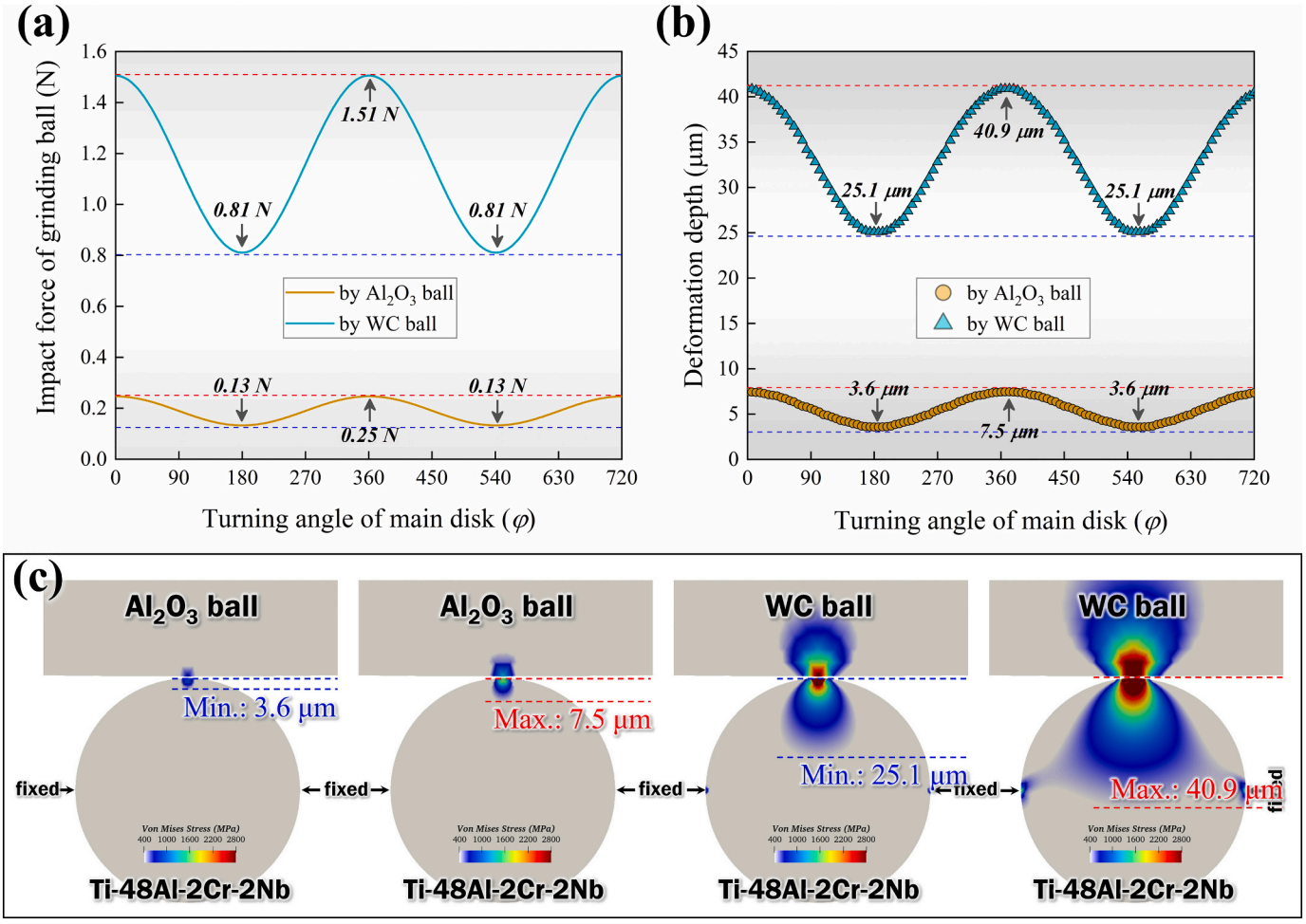

Fig. 5. (a) Impact force of grinding balls during ball milling, (b) deformation depth of GA Ti–48Al–2Cr–2Nb, and (c) snapshots of contact mechanic simulations using Al_2O_3 and WC balls.

the formation of the fractured flakes with an irregular surface.

3.2. Deformation mechanism depending on ball milling media

To clarify the deformation mechanism of the GA powder during ball milling depending on the grinding media, the numerical calculation model was developed based on the Hertzian contact theory. During ball milling, the position taken by the grinding ball at an arbitrary time moment can be approximated by [30]:

$$R(t) = r_d^2 + r_v^2 + 2r_d r_v cos[4\pi\omega t(k+1)] \quad (6)$$

where r_d and r_v are the radii of the main disk and milling vial in the ball mill, respectively, ω is the angular velocity of the main disk, and k is the speed coefficient of the rotating vial. Based on the turning angle of the main disk ($\varphi = 2\pi\omega t$), the impact force of the grinding ball, which acts on a powder particle or the mill wall, can be expressed by:

$$F(t) = 4\pi^2 m\omega^2 R(t) \quad (7)$$

where m is the weight of Al_2O_3 (0.27 g) and WC (1.65 g) grinding balls. The calculated impact force of grinding balls during rotation is presented in Fig. 5a. The impact force continuously changes during ball milling, and the maximum impact force of the WC ball is about 6 times higher than that of the Al_2O_3 ball because of heavier weight. The contact mechanical analysis was conducted to evaluate the collision stress during ball milling depending on the grinding media. The detailed numerical equation for contact mechanical simulation can be found in the previous study [24,26]. The mechanical deformation depth of Ti–48Al–2Cr–2Nb powder was estimated using the general tensile strength (400 MPa) of bulk alloy. The maximum deformation depth by WC ball is 40.9 μm, which is almost 5.5 times that by Al_2O_3 ball (7.5 μm), as shown in Fig. 5b and c. As discussed in the previous section, the surface-attached satellites in the GA powder were removed, and the shape factor decreased after Al_2O_3 ball milling, indicating a smooth surface. Furthermore, the nanoscale surface roughness slightly increased after Al_2O_3 ball milling, while the fraction of spherical particles remained above 0.5. This result indicates that the Al_2O_3 ball milling at 400 rpm could be insufficient to pulverize the GA powder owing to low impact force. Thus, surface grinding predominantly occurred without particle fracture during Al_2O_3 ball milling. In contrast, after WC ball milling, fine flake-shaped particles were observed, and the shape factor increased indicating an irregular surface. The nanoscale surface roughness significantly increased to 147.2 nm, while the fraction of elongated particles increased to 0.67. In the contact mechanical simulation, the maximum deformation depth by the WC ball was about 5.5 times that by the Al_2O_3 ball. It is well known that the α_2-Ti_3Al is the brittle phase in the TiAl alloy system because of its intermetallic character and limited slip system on $\langle 11\bar{2}0\rangle\{10\bar{1}0\}$ [31]. Thus, the brittle fracture of the GA powder could be favorable during WC ball milling at 400 rpm, thus leading to predominantly pulverization owing to the high impact force.

3.3. Effect of ball milling on flowability

The mass flow rate and static AOR of the GA and ball-milled powders

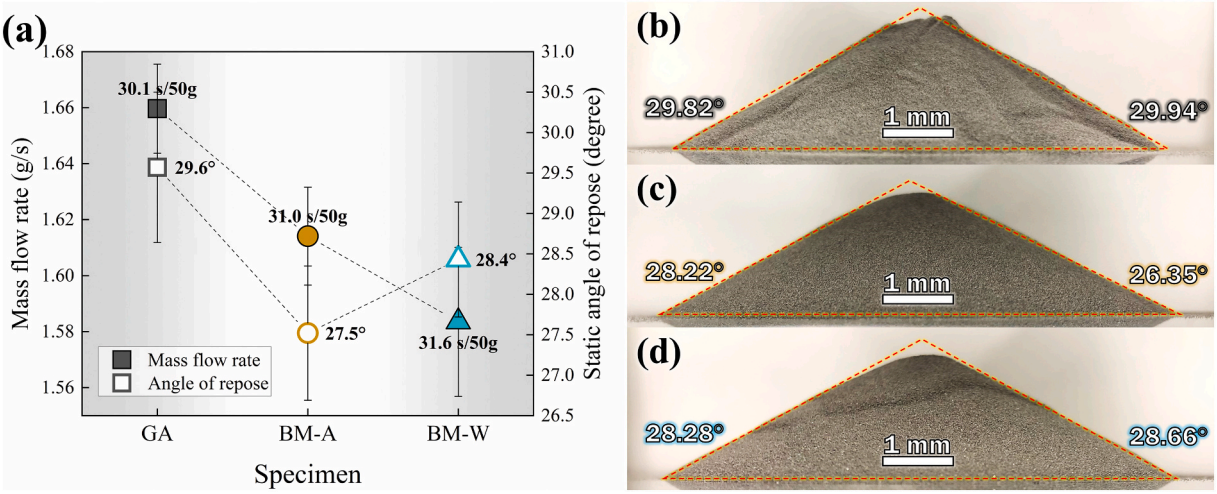

Fig. 6. (a) Mass flow rate and static AOR of deposited powder piles of Ti–48Al–2Cr–2Nb powders: (b) GA, (c) BM-A, and (d) BM-W.

obtained by the Hall flowmeter test are presented in Fig. 6a–d. The mass flow rate of the GA powder (1.66 g/s) decreased to 1.61 g/s after ball milling with Al_2O_3, indicating a decrease in flowability despite the removal of surface satellites. At the same time, the mass flow rate decreased to 1.22 g/s after ball milling with WC (Fig. 6a). The flowability of coarse particles has been reported to be higher than that of fine particles because of the smaller surface area [32]. Mussatto pointed out that the satellite-containing particles can decrease the flowability because of higher mechanical interlocking compared to spherical or elongated particles [18]. Yablokova et al. demonstrated that irregular-shaped particles can deteriorate flowability owing to high interparticle friction [33]. This result indicates that the decreased flowability in the BM-W powder could be attributed to the increase in the fraction of fine and irregular particles via brittle fracture. At the same time, the gravity-induced flowability of BM-A powder was lower than that of the GA powder despite their similar PSDs and the removal of satellites. The surface roughness of particles is one of the factors through which the flowability may be controlled. Tay et al. reported that rougher particles showed poorer compressibility and particle flow owing to the higher interparticle friction for particle motion [34]. In the BM-A powder, nanoscale surface roughness increased owing to locally repeated deformation via ball milling. Thus, the decrease in the gravity-induced

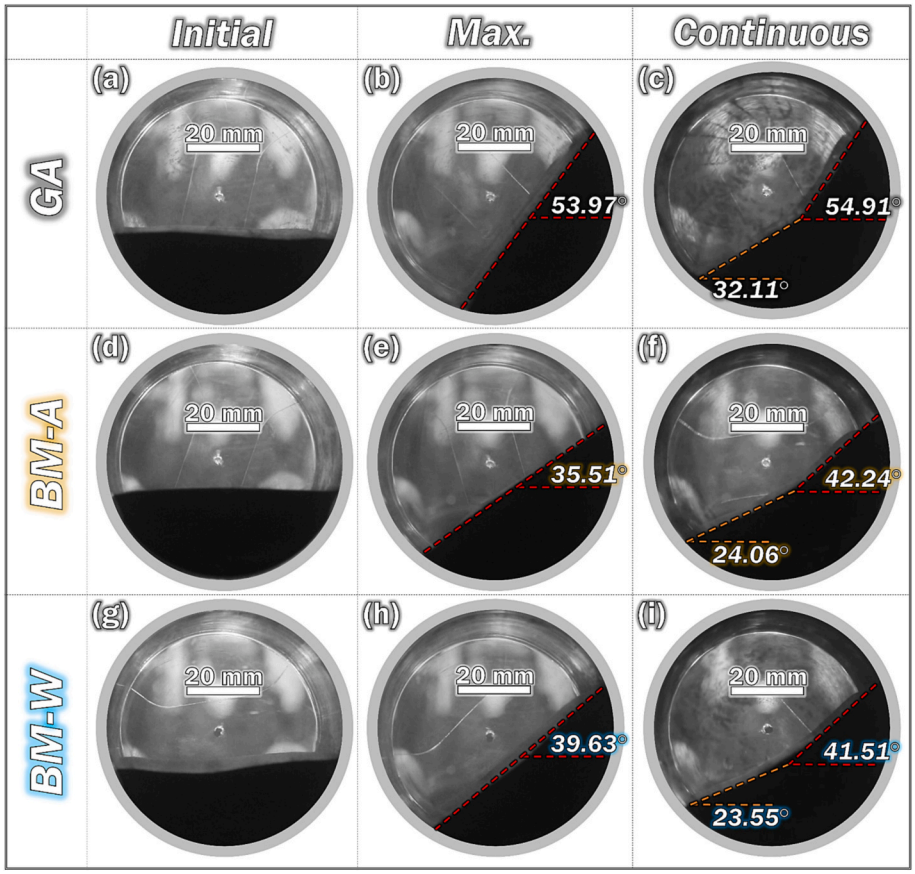

Fig. 7. Snapshots of the rotating drum tests of Ti–48Al–2Cr–2Nb powders: (a)–(c) GA, (d)–(f) BM-A, and (g)–(i) BM-W.

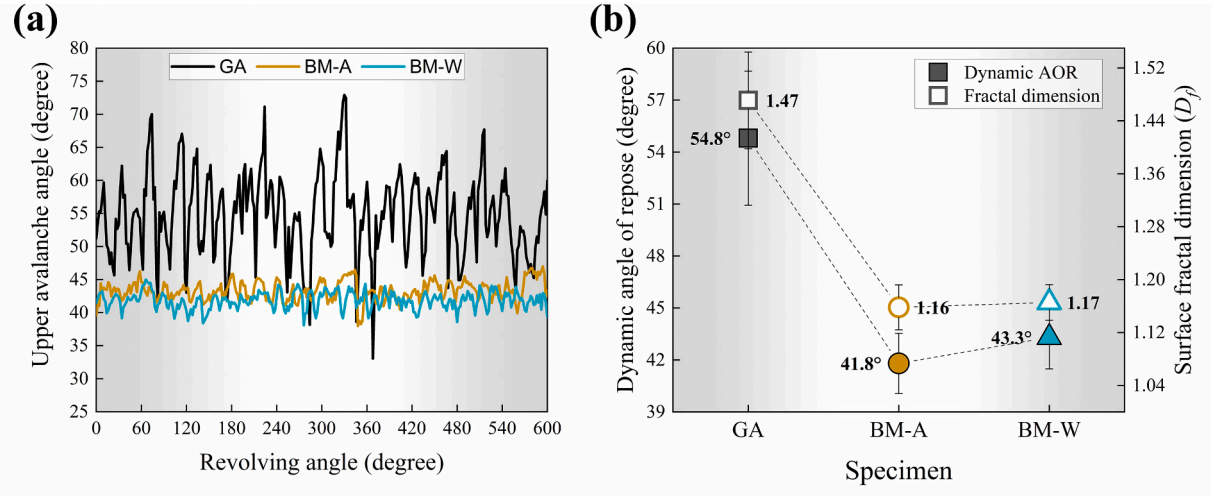

Fig. 8. (a) Avalanche angle variation in the rotating drum test, (b) dynamic AOR and surface fractal dimension of the GA and ball-milled powders.

flowability of the BM-A powder could be attributed to the increased interparticle friction because of high surface roughness. At the same time, the static AOR in the GA powder is the highest (29.8°) despite improved flowability, while it is 27.5 and 28.4° for BM-A and BM-W, respectively (Fig. 6b–d). Interestingly, a conical pile of the GA powder had a wavy surface, while this was not observed for the BM-A and BM-W powders. Gärtner et al. reported that the wavy surface in powder pile is mainly attributed to cohesion force, and it can be suppressed by increasing surface roughness owing to decreased van der Waals force using a dry surface coating [21]. This result suggests that the high static AOR of GA powder could be contributed by high cohesion force despite rough surface. Therefore, it can be deduced that the cohesion force of GA powder could be not attributed to van der Waals force, but there are other factors to increase cohesion force.

The snapshots of the rotating drum test using the GA and ball-milled powders are presented in Fig. 7a–i. In the initial state, 30 vol% of the rotating drum was filled with the tested powder. The drum was then rotated up to maximum avalanche slope, which showed the interparticle friction and cohesive force that prevented the collapse because of the gravitational force. The maximum avalanche angle of the GA powder is the highest at 54.0°, and BM-A and BM-W powders show significantly lower values of 35.5 and 39.6°, respectively. As the drum was further rotated, the powder formed a continuous flow regime, and the angle variation was obtained using continuous image analysis. The recorded videos of the rotating drum tests of the GA and ball-milled powders are presented in Supplementary video 1. The variation in the avalanche angle during the rotation of the GA and ball-milled powders is presented in Fig. 8a. The avalanche angle of the GA powder fluctuates, which represents the cascading flow, and the dynamic AOR is 54.8°. The fluctuations in avalanche angle are much lower in the BM-A and BM-W powders, which is similar to the rolling flow, and their dynamic AOR values are 41.8 and 43.3°, respectively (Fig. 8b). The surface fractal dimension (D_f) of the powder in the rotating drum test can be expressed by [35]:

$$L(\varepsilon) = M\varepsilon^{(1-D_f)} \tag{8}$$

where L is the total length of free surface of the powder during rotation, ε is the measurement scale for free surface, M and D_f are constants determined by fitting at various measurement scales. In the fractal analysis of the rotating drum test, $D_f = 1$ indicates the perfectly smooth surface without agglomeration, while the $D_f > 1$ indicates the fluctuating surface that causes powder agglomeration [36]. Thus, D_f represents the cohesive force of the powder under the rotating conditions. The D_f of the

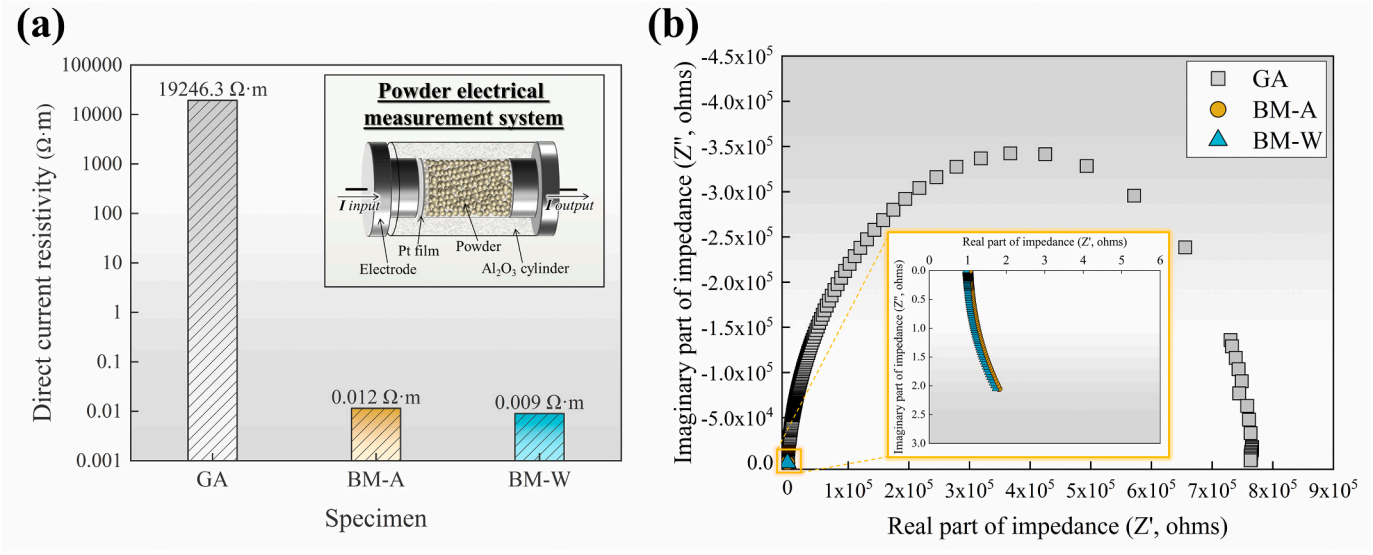

Fig. 9. (a) Direct current resistivity and (b) alternating current impedance test results for the GA and ball-milled powders.

Table 2
Electrical properties of the GA and ball-milled Ti–48Al–2Cr–2Nb powders.

Specimen	DC resistivity [Ω·m]	Resistance of metallic matrix [Ω]	Resistance of oxide film [Ω]	Charge dissipation time [μm]
GA	19,246.3	1.131	763,792	55.95
BM-A	0.012	1.057	1.814	–
BM-W	0.009	0.959	1.722	–

GA powder is 1.47, indicating cohesive characteristics under rotating conditions, while for the BM-A and BM-W powders it is almost 1.16 and 1.17, respectively, indicating a smooth surface (Fig. 8b). This result suggests that the cohesive force is significantly higher in the GA powder than in the ball-milled powders under rotating conditions.

3.4. Electrical and surface properties

The DC resistivity and AC impedance test results for the GA and ball-milled powders are presented in Fig. 9a and b. The DC resistivity of the GA powder (19,246.3 Ω·m) is much higher than those of the BM-A (0.012 Ω·m) and BM-W (0.009 Ω·m) powders (Fig. 9a). In the AC impedance test, the capacitive response is observed in the GA powder, and the electrical resistance of the oxide film is 763,792 Ω (Fig. 9b). In contrast, the inductive response representing metal-like electrical conductivity is observed in the BM-A and BM-W powders, and their electrical resistances of the oxide film are similar to those of metallic core parts, as shown in Table 2. The further detailed theory of an equivalent electrical circuit for powder can be found in the previous study [24–26]. These results indicate that the electrical resistance of the oxide film in the GA powder was significantly decreased by ball milling.

The survey and high-resolution spectra of the GA and ball-milled powders are presented in Fig. 10a and b. The surface spectra of the GA and ball-milled powders are similar, indicating that the chemical composition of the oxide film did not change after ball milling (Fig. 10a).

As mentioned previously, the oxygen concentration of GA powder was preserved after Al_2O_3 and WC ball milling (Table 1). Thus, the elimination of oxide film by surface grinding is negligible in ball-milled powders. In the high-resolution Ti *2p* spectrum, the Ti^{3+} and Ti^{2+} peaks in BM-A and BM-W powders have higher intensities than those in the GA powder owing to the deformation accumulation on the oxide film during ball milling, as shown in Table 3. It is well known that the electrical conductivity of Ti suboxide resembles that of the metallic material because of the presence of oxygen vacancies acting as free electrons [37]. In the previous studies, the electrical resistance of the oxide film containing 3d transition-metal oxides was significantly decreased via mechanical deformation, and the capacitive response disappeared because of metal–insulator transition caused by the accumulation of strain and/or defects in the oxide film [24–26]. Thus, in the present study on Ti–48Al–2Cr–2Nb, the metal-like electrical resistance of the BM-A and BM-W powders may be attributed to the increase in the number of oxygen vacancies in the oxide film because of mechanical deformation, and the capacitor component could be replaced by an inductor via deformation-induced metal–insulator transition.

3.5. Factor determining cohesive force

As discussed in the previous section, the cohesive force under the dynamic conditions was significantly higher in the GA powder than in

Table 3
Atomic concentration in powder surface of the GA and ball-milled Ti–48Al–2Cr–2Nb powders.

Specimen	Atomic concentration of oxide surface (at.%)						
	O^{2-}	Ti^{4+}	Ti^{3+}	Ti^{2+}	Al^{3+}	Cr^{3+}	Nb^{5+}
GA	65.03	8.43	0.98	0.55	23.82	0.91	0.28
BM-A	62.73	8.41	2.11	1.42	24.11	0.85	0.37
BM-W	62.79	8.51	1.89	1.92	23.78	0.77	0.34

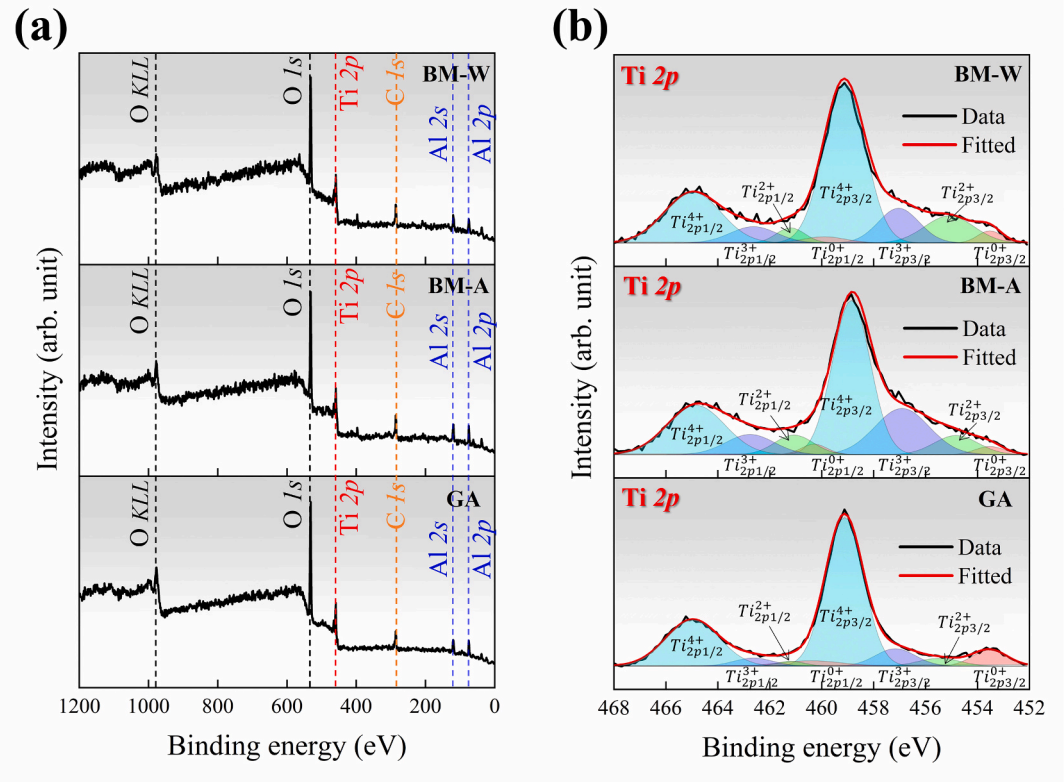

Fig. 10. Survey and high-resolution Ti *2p* spectra of the GA and ball-milled powders.

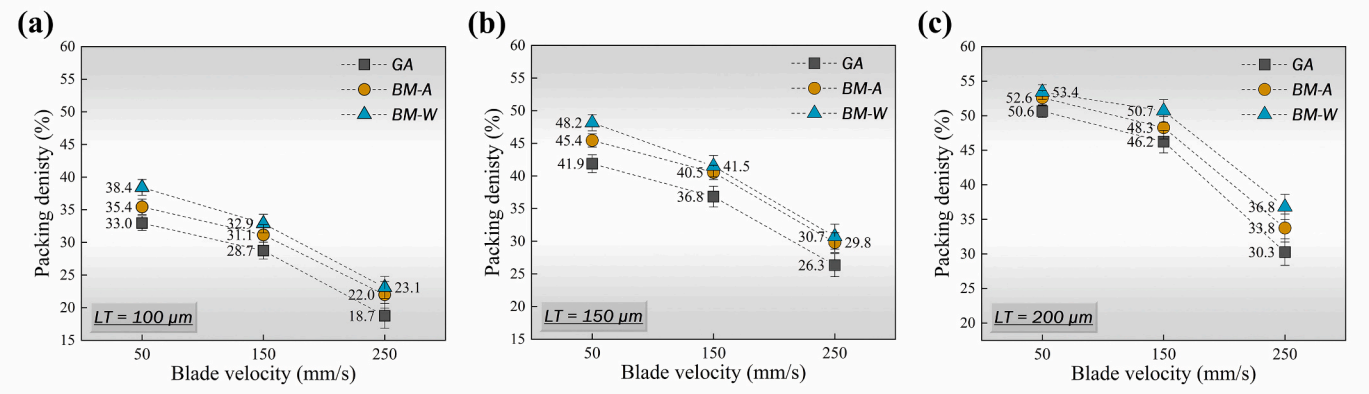

Fig. 11. Packing density of the GA and ball-milled powders depending on the spreading velocity at a layer thickness of (a) 100 μm, (b) 150 μm, and (c) 200 μm.

the ball-milled powders. The cohesive force causing the agglomeration of the powder may be caused by several factors, such as van der Waals, electrostatic, capillary, and magnetic forces [38]. The humidity and magnetic field were very weak in the powder flowability test; thus capillary and magnetic forces were negligible. Several studies reported that the van der Waals force is the predominant cohesive factor for the powder flowability and spreading process [39–41]. The van der Waals force in the powder can surpass the gravitational force at a sufficiently small particle size [41]. Spurek et al. reported that the surface fractal in the rotating drum test significantly increased with decreasing mean particle size below 20 μm in 316 L powder [36]. However, the mean particle size of the GA powder was 68.87 μm, which is considerably higher than that of the BM-W powder, even though the cohesive force was higher in the GA powder. This suggests that the van der Waals force is a minor factor in the increase in the cohesive force in the GA powder under dynamic conditions. Therefore, the cohesive force under dynamic conditions may be predominantly caused by the electrostatic force through triboelectric charging and the formation of a potential difference [42]. The electrostatic force (F_c) between the charged and uncharged particles at a certain distance can be expressed using the classical Coulomb Eq. [43]:

$$F_c = \frac{Q^2\left(1-\frac{d}{\left(r^2+d^2\right)^{1/2}}\right)}{16\pi\varepsilon_0 d^2} \tag{9}$$

where Q is the particle charge, d is the distance between the particles, r is the equilibrium radius of the particle, and ε_0 is the vacuum permittivity (8.854×10^{-12} F·m^{-1}). In the previous study, it was confirmed that the GA Ti–48Al–2Cr–2Nb powder consisted of resistor–capacitor circuits owing to the core–shell structure of the particles: a metallic matrix encapsulated by an oxide film [24]. Thus, the charging degree of the powder containing resistor–capacitor circuit can be expressed by [43]:

$$Q = CV_C = CV_S\left(1-e^{(-t/\tau)}\right) \tag{10}$$

where C is capacitance, V_C is the voltage across the capacitor, V_S is the supply voltage, t is the duration after the supply voltage, and τ is the charge dissipation time. The charge dissipation time equals the product of the capacitance and resistance of the oxide film acting as a capacitor [44]. This result suggests that the charge accumulation on the oxide film could result in a high electrostatic force between the particles owing to the long-term charge retention. In the DC resistivity measurement, the electrical resistance of GA powder was the highest, while it was significantly lower in the BM-A and BM-W powders (Fig. 9a). As shown in the XPS results, the quantity of Ti suboxide on the oxide film increased after ball milling with both media owing to the accumulation of deformations (Fig. 10b). It has been reported that the resistance of oxide films can be decreased by increasing the oxygen vacancy density on the powder surface via mechanical stimulation [24–26]. Furthermore, the resistor–capacitor circuit in the GA powder changed to the resistor–inductor circuit in the BM-A and BM-W powders via deformation-induced metal–insulator transition (Fig. 9b). This result suggests that the charge accumulation in the BM-A and BM-W powders was limited because of their particles did not act as capacitors. Therefore, triboelectric charge can be accumulated in the GA powder under the dynamic conditions owing to the long charge dissipation time. The cohesive force in the GA powder is mainly attributed to the electrostatic force caused by the dielectric properties of the oxide film. On the other hand, the triboelectric charging of GA powder under static conditions (i.e. gravity) could be suppressed due to insufficient particle interaction. Therefore, it can be deduced that the gravity-induced flowability of GA powder is minorly affected by cohesive force caused by triboelectric charging and is mainly contributed by nanoscale surface roughness (Figs.3 and 6). Recently, Zhao et al. reported that the nanoscale surface roughness is the main factor determining flowability using three types of Inconel 718 powder, which were produced by gas atomization, plasma atomization, and plasma rotating electrode process; they also showed that the avalanche angle in the rotating drum test increased with oxide film thickness [45]. Considering the obtained results, oxide film thickness rather than surface roughness was considered the controlling factor determining the flowability of the powder because of the high electrostatic force caused by the long-term charge retention. Therefore, the cohesive effect of the electrostatic force was demonstrated to be the predominant factor controlling the flowability of the GA powder under dynamic conditions.

3.6. Factor determining powder bed quality and spreadability

The powder spreading test was conducted to determine the critical factor affecting the packing density and spreadability in the powder bed fusion-based additive manufacturing process. The packing density at a layer thickness of 100 μm in the GA and ball-milled powders depending on the spreading velocity is presented in Fig. 11a. The packing density of the powders is the highest at 50 mm/s and rapidly decreases with increasing spreading velocity. The packing density of the BM-W powder is the highest (38.4%) at a spreading velocity of 50 mm/s, while that of the GA powder is the lowest (33%). As mentioned above, the BM-W powder exhibited the smallest mean particle size of 45.72 μm, while those of the GA and BM-A powders were similar (68.87 and 60.65 μm, respectively). However, the shape factor of the BM-W powder was the highest indicating irregular particle morphology owing to the brittle fracture via ball milling. Nan et al. demonstrated that high interparticle friction can improve the packing density due to the suppressed particle motion during the powder spreading process [46]. This result indicates that the kinetic energy of BM-W powder more rapidly dissipated compared to GA and BM-A powders in powder spreading process.

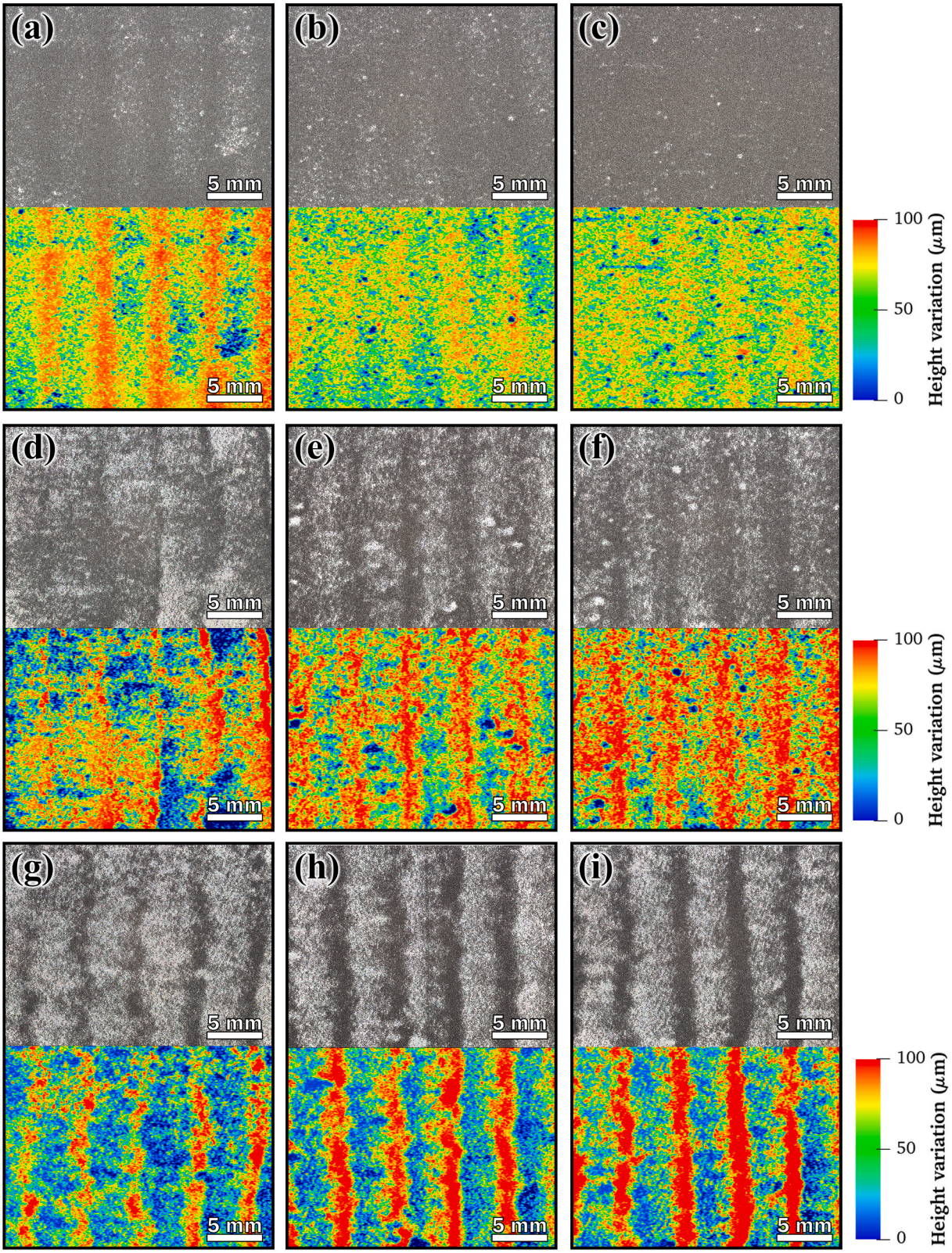

Fig. 12. Deposited powder beds of Ti–48Al–2Cr–2Nb powders at a layer thickness of 100 μm under different spreading velocities: (a), (d), (g) GA, (b), (e), (h) BM-A, and (c), (f), (i) BM-W powders. Spreading velocities: (a)–(c) 50 mm/s, (d)–(f) 150 mm/s, (g)–(i) 250 mm/s.

Haferkamp et al. reported that the fine particle is advantageous to minimize the wall effect in the powder spreading with a thin layer thickness [47]. Thus, the surface pores of deposited powder bed could be suppressed in BM-W powder than in GA and BM-A powders owing to the decreased kinetic energy and minimized wall effect. On the other hand, Yim et al. reported that the irregular particle shape can decrease the packing density of the powder bed because of the increased pore size and number caused by sharp edge contact [26]. Zhu et al. demonstrated that

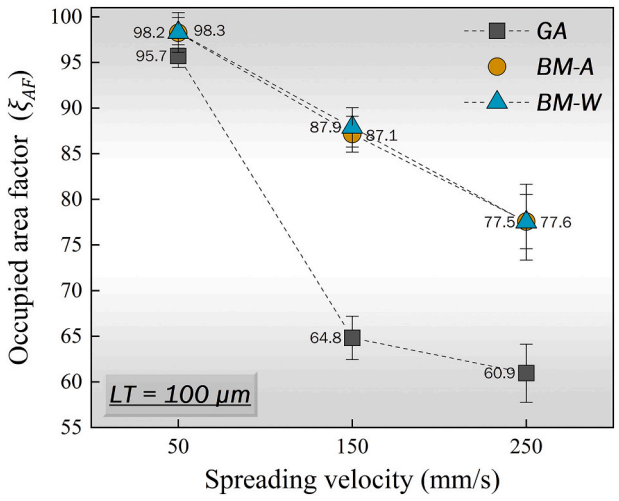

Fig. 13. Measured occupied area factor in deposited powder beds of Ti–48Al–2Cr–2Nb powders at a layer thickness of 100 μm.

the addition of fine particles can improve the packing density because of the void filling effect in the deposited powder bed [48]. This result suggests that the void filling effect by fine particle could be more dominant than void increase effect by irregular particle in a deposited BM-W powder bed. Therefore, the highest packing density of BM-W powder bed at a layer thickness of 100 μm was attributed to the decreased surface and inside pores.

The images of the deposited powder beds of the GA and ball-milled powders with a layer thickness of 100 μm at different spreading velocities are presented in Fig. 12a–i. The homogeneous distribution without large defects is observed in the BM-A and BM-W powder beds at a spreading velocity of 50 mm/s, while the unoccupied area is observed in the GA powder bed. At the spreading velocity of 150 mm/s, the wave-like height variation is observed in all powder beds owing to the temporally decreased spreading velocity because of the stepping motor motion. The height variation in powder beds increases with spreading velocity, and the maximum height, observed at the spreading velocity of 250 mm/s, is >100 μm, which was set as layer thickness in the powder spreading experiment. This result implies that the deposited powders could prolong the particle flow after deposition under high spreading velocities. In the deposited powder bed, the spreadability of the powder can be expressed based on the occupied area factor (ξ_{AF}) as follows:

$$\xi_{AF} = \frac{A_{PB}}{A_{Total}} \tag{11}$$

where A_{PB} and A_{Total} are the occupied and total observation areas in the deposited powder bed, respectively. The measured ξ_{AF} in deposited powder beds at a layer thickness of 100 μm is presented in Fig. 13. The ξ_{AF} values in the BM-A and BM-W powders are similar at a spreading velocity of 50 mm/s, while it is lower in the GA powder. The ξ_{AF} values of the BM-A and BM-W powders gradually decreases with increasing spreading velocity, while that of the GA powder decreases more rapidly. This result suggests that the spreadability of the BM-A and BM-W powders is superior to that of the GA powder. Interestingly, the packing density and spreadability of the BM-A powder are superior to that of the GA powder despite similar PSDs. As discussed in the previous section, the cohesion force under dynamic conditions was considerably higher in the GA powder than in the BM-A and BM-W powders because of the high electrostatic force caused by its capacitive properties. Furthermore, the shape factor of the GA powder decreased after ball milling with Al_2O_3, indicating a smoother surface and more spherical shape, because of the removal of surface-contained satellites via surface grinding. Chen et al. reported that the cohesion force can significantly decrease the packing density during powder spreading owing to the particle agglomeration [49]. It is well known that the presence of satellites on the surface can increase the particle interlocking during powder spreading, resulting in a low packing density because of an increase in pore size [18,50]. This indicates that the packing density and spreadability of the GA powder could be decreased by high cohesion force and particle interlocking compared to the BM-A powder.

The packing density of the powder beds gradually increased with a layer thickness under the spreading velocity of 50 mm/s. Particularly, the packing densities of the powder beds are >40% higher (compared to those at 100 μm) at a layer thickness >150 μm (Fig. 11b and c). Nan et al. reported that the decrease in flowability can improve the packing density by suppressing particle motion during powder spreading [46]. In the previous study, the rapid stress dissipation during powder spreading was confirmed to improve the packing density owing to the suppression of force-arch formation [19]. This indicates that the increase in layer thickness could increase the number of inter-particle interactions resulting the rapid kinetic energy dissipation. Wu et al. demonstrated that application of the additional compressive force during powder spreading can improve the packing density of the deposited powder bed [51]. During spreading, the high layer thickness leads to the increase in the compressive force exerted by the upper deposited powder layer. Furthermore, the wall effect can be minimized as increasing layer thickness in powder spreading process [47]. Based on the obtained results, the increase in packing density with layer thickness in powder spreading was attributed to the synergetic effect of rapid energy dissipation, increased compressive force, and decreased wall effect.

The deposited powder beds of the GA and ball-milled powders at a layer thickness of 150 μm under different spreading velocities are shown in Fig. 14a–i. The deposited powders are homogeneously distributed on the base plates without an unoccupied region at a layer thickness of 150 μm, while the height variation is higher at a spreading velocity of 250 mm/s. However, the evaluation of spreadability using ξ_{AF} was difficult because of the homogeneous deposition of particles on the base plate even at a spreading velocity of 250 mm/s, as shown in Fig. 14g–i. The surface roughness of the powder bed is one of the factors representing the spreadability of the powder in the powder spreading process [19]. The surface roughness (ξ_{SR}) was determined in the center region of the deposited powder bed, as shown in Fig. 15a. The ξ_{SR} values of the powder beds with different layer thicknesses are presented in Fig. 15b–d. Although the differences in ξ_{SR} between the powders are not significant at a spreading velocity of 50 mm/s, they increase with spreading velocity under various layer thicknesses. The general trend is that the ξ_{SR} of the GA powder is higher than that of the BM-A and BM-W powders under various layer thicknesses and spreading velocities, representing low spreadability. This result suggests that the spreadability of the GA powder is mainly affected by cohesion caused by high electrostatic force; however, the spreadability may be improved through the suppression of charge accumulation, caused by deformation-induced metal–insulator transition, via ball milling. Overall, it was demonstrated that the packing density and spreadability of the GA powder can be improved by controlling the particle size, morphology, and surface properties via ball milling.

4. Conclusion

In this study, ball milling was used to improve the flowability and powder bed properties of GA Ti–48Al–2Cr–2Nb powder in the PBF-AM process. The main conclusions drawn from this study are as follows.

1) The deformation mechanism of the GA powder during ball milling was investigated depending on the ball milling media. The mean particle diameter of the GA powder slightly decreased after Al_2O_3 ball milling and significantly decreased after WC ball milling. The spherical shape of particles was preserved after Al_2O_3 ball milling, while flake particles with irregular shapes were observed after WC ball milling. The contact mechanic simulation results suggested that the brittle fracture of the GA powder was favorable during WC ball milling at 400 rpm owing to the

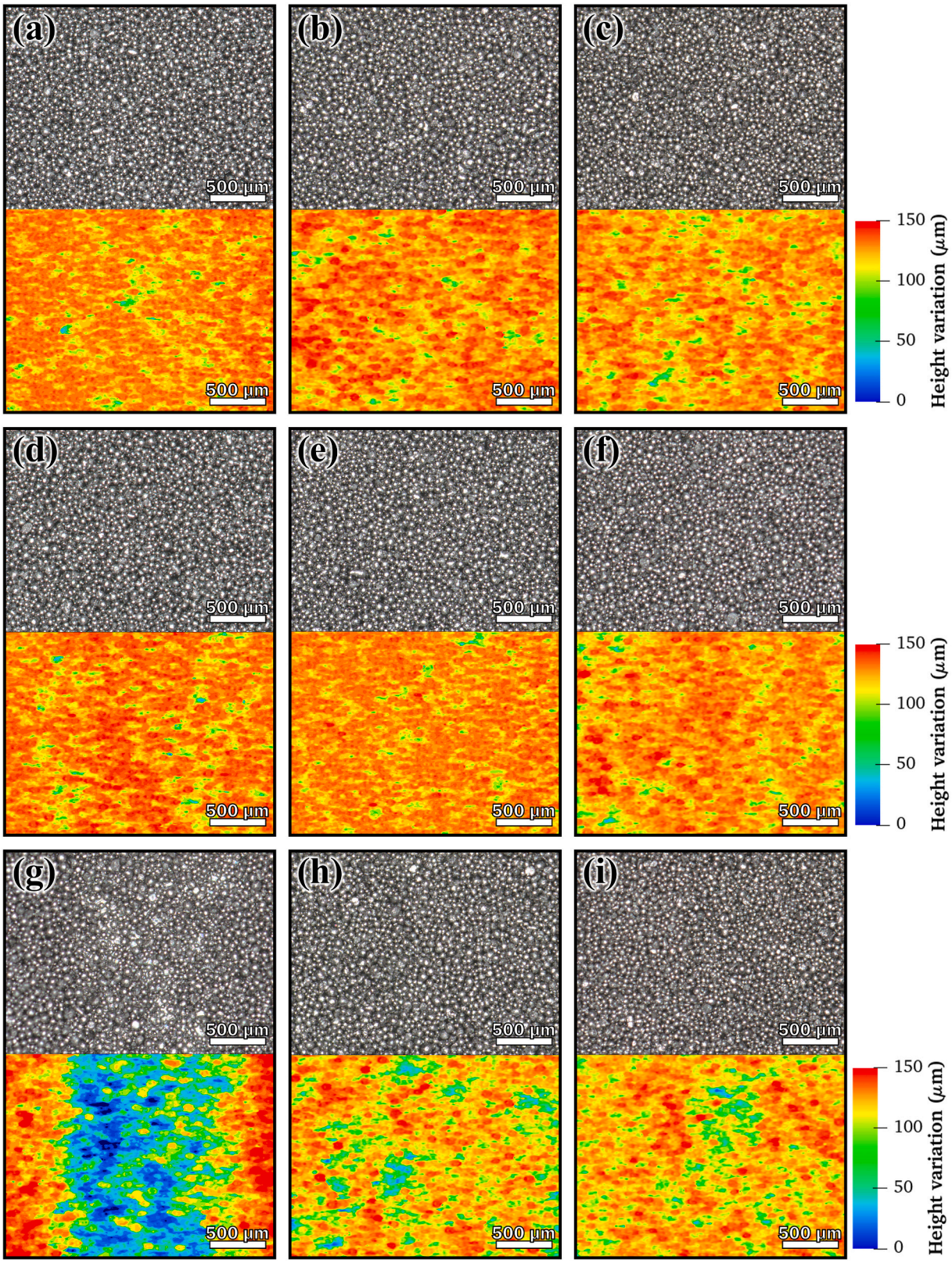

Fig. 14. Deposited powder beds of Ti–48Al–2Cr–2Nb powders at a layer thickness of 150 μm under different spreading velocities: (a), (d), (g) GA, (b), (e), (h) BM-A, and (c), (f), (i) BM-W powders. Spreading velocities: (a)–(c) 50 mm/s, (d)–(f) 150 mm/s, and (g)–(i) 250 mm/s.

high impact force.

2) The effect of ball milling on the flowability of the GA powder was examined using the Hall flowmeter and rotating drum tests. The gravity-induced flowability of the GA powder decreased after ball milling owing to the increased interparticle friction caused by high surface roughness of the particles. The rotation-induced flowability of the GA powder was considerably improved by ball milling owing to the decrease in the cohesive force. The cohesive force in the GA powder is primarily

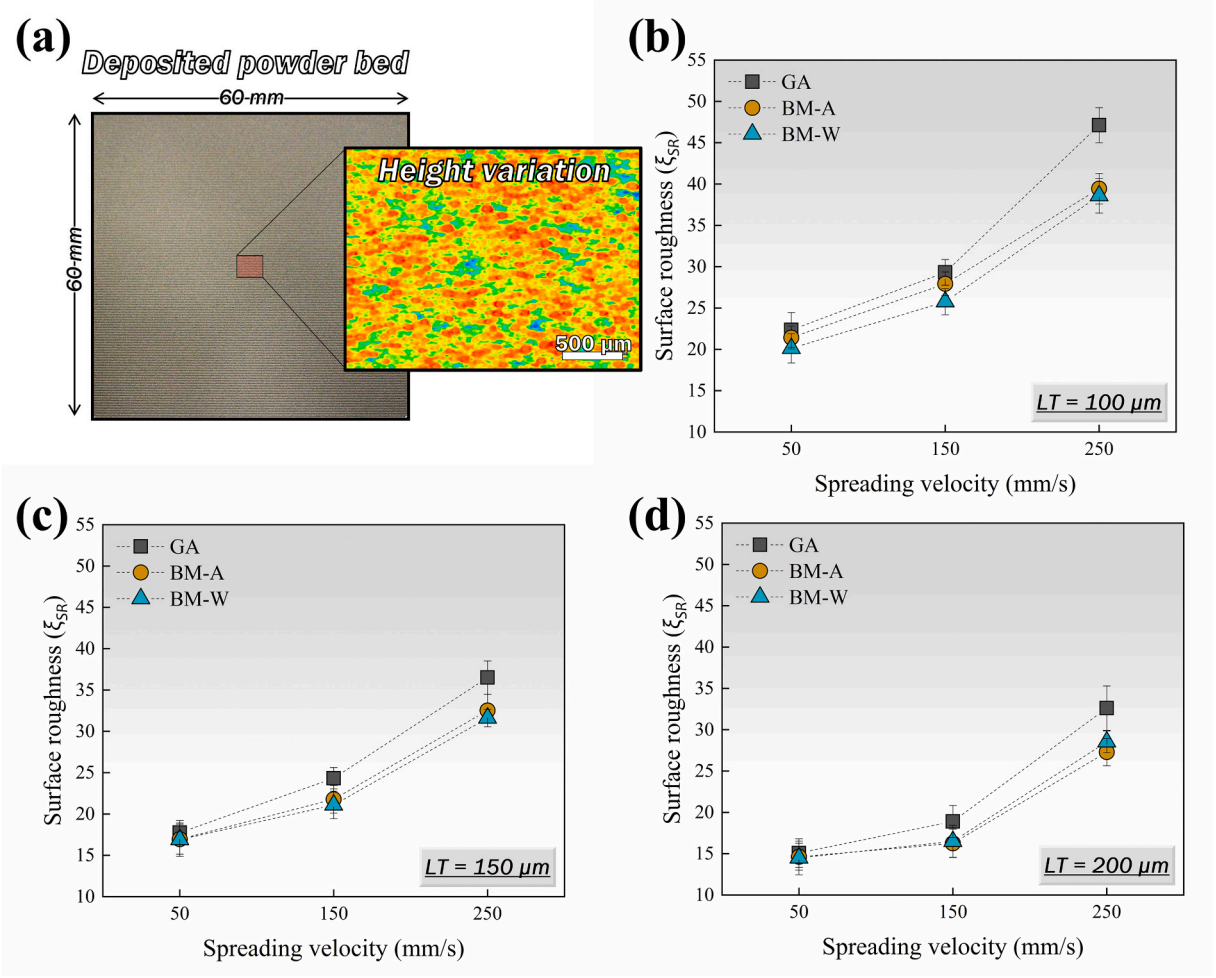

Fig. 15. (a) Schematic for measuring surface roughness of the powder bed and measured surface roughness of Ti–48Al–2Cr–2Nb powders at a layer thickness of (b) 100 μm, (c) 150 μm, and (d) 200 μm.

constituted by the electrostatic force caused by the charge accumulation under dynamic conditions.

3) The packing density and spreadability of the GA powder were optimized using ball milling. The packing density of the GA powder increased after WC ball milling because of the combined effect of rapid energy dissipation, minimized wall effect, and void filling effect. The spreadability of the GA powder was limited because of the cohesive force caused by electrostatic force; however, it can be improved by eliminating the capacitor component via deformation-induced metal–insulator transition using ball milling.

Overall, it was demonstrated that the flowability and spreadability of GA Ti–48Al–2Cr–2Nb powder can be improved by manipulating the particle size, morphology, and surface propertyies via ball milling.

Supplementary data to this article can be found online at https://doi.org/10.1016/j.powtec.2022.117996.

CRediT authorship contribution statement

Seungkyun Yim: Conceptualization, Methodology, Software, Investigation, Writing – original draft, Visualization. **Kenta Aoyagi:** Writing – review & editing, Supervision, Resources. **Huakang Bian:** Investigation, Writing – review & editing, Supervision, Resources. **Yujie Cui:** Writing – review & editing. **Akihiko Chiba:** Writing – review & editing, Supervision, Funding acquisition, Project administration.

Declaration of Competing Interest

The authors declare that they have no known competing financial interests or personal relationships that could have appeared to influence the work reported in this paper.

Data availability

The authors are unable or have chosen not to specify which data has been used.

Acknowledgements

This work was partially supported by JSPS KAKENHI [grant number 18H05455]. This research was also partially supported by Materials Integration for Revolutionary Design System of Structural Materials of the Cross-Ministerial Strategic Innovation Promotion Program (SIP) of Japan Science and Technology (JST). This work was partly supported by the Technology Research Association for Future Additive Manufacturing (TRAFAM). This work was also partly supported by the Innovative Structural Materials Association (ISMA) commissioned by the New Energy and Industrial Technology Development Organization (NEDO). The authors also thank Sato Tsukasa, Institute for Materials Research, Tohoku University, for manufacturing the powder spreading device.

References

[1] J.C. Najmon, S. Raeisi, A. Tovar, Review of Additive Manufacturing Technologies and Applications in the Aerospace Industry, Elsevier Inc., 2019, https://doi.org/10.1016/B978-0-12-814062-8.00002-9.

[2] X. Zhang, E. Liang, Metal additive manufacturing in aircraft: current application, opportunities and challenges, IOP Conf. Ser. Mater. Sci. Eng. 493 (2019), https://doi.org/10.1088/1757-899X/493/1/012032.

[3] M. Rahman, D. Brackett, K. Milne, A. Szymanski, A. Okioga, L. Huertas, S. Jadhav, An integrated process and data framework for the purpose of knowledge management and closed-loop quality feedback in additive manufacturing, Prog. Addit. Manuf. (2022), https://doi.org/10.1007/s40964-021-00246-7.

[4] A. Gisario, M. Kazarian, F. Martina, M. Mehrpouya, Metal additive manufacturing in the commercial aviation industry: a review, J. Manuf. Syst. 53 (2019) 124–149, https://doi.org/10.1016/j.jmsy.2019.08.005.

[5] C. Körner, Additive manufacturing of metallic components by selective electron beam melting - a review, Int. Mater. Rev. 61 (2016) 361–377, https://doi.org/10.1080/09506608.2016.1176289.

[6] C.D. Boley, S.A. Khairallah, A.M. Rubenchik, Calculation of laser absorption by metal powders in additive manufacturing, Appl. Opt. 54 (2015) 2477, https://doi.org/10.1364/ao.54.002477.

[7] Y.S. Lee, W. Zhang, Mesoscopic simulation of heat transfer and fluid flow in laser powder bed additive manufacturing, Int. Solid Free Form Fabr. Symp. (2015) 1154–1165, utw10945.utweb.utexas.edu/sites/default/files/2015/2015-94-Lee.pdf.

[8] Y. Zhao, H. Bian, H. Wang, K. Aoyagi, K. Yamanaka, A. Chiba, Non-equilibrium solidification behavior with solute trapping associated with powder characteristics during electron beam additive manufacturing, Mater. Des. 221 (2022), 110915, https://doi.org/10.1016/j.matdes.2022.110915.

[9] Y. Zhao, K. Aoyagi, Y. Daino, K. Yamanaka, A. Chiba, Significance of powder feedstock characteristics in defect suppression of additively manufactured Inconel 718, Addit. Manuf. 34 (2020), 101277, https://doi.org/10.1016/j.addma.2020.101277.

[10] Y. Zhao, Y. Koizumi, K. Aoyagi, K. Yamanaka, A. Chiba, Thermal properties of powder beds in energy absorption and heat transfer during additive manufacturing with electron beam, Powder Technol. 381 (2021) 44–54, https://doi.org/10.1016/j.powtec.2020.11.082.

[11] A.M. Rausch, V.E. Küng, C. Pobel, M. Markl, C. Körner, Predictive simulation of process windows for powder bed fusion additive manufacturing: influence of the powder bulk density, Materials (Basel). 10 (2017), https://doi.org/10.3390/ma10101117.

[12] S. Diener, A. Zocca, J. Günster, Literature review: methods for achieving high powder bed densities in ceramic powder bed based additive manufacturing, Open Ceram. 8 (2021), 100191, https://doi.org/10.1016/j.oceram.2021.100191.

[13] L. Cao, Study on the numerical simulation of laying powder for the selective laser melting process, Int. J. Adv. Manuf. Technol. 105 (2019) 2253–2269, https://doi.org/10.1007/s00170-019-04440-4.

[14] D. Yao, X. Liu, J. Wang, W. Fan, M. Li, H. Fu, H. Zhang, X. Yang, Q. Zou, X. An, Numerical insights on the spreading of practical 316 L stainless steel powder in SLM additive manufacturing, Powder Technol. 390 (2021) 197–208, https://doi.org/10.1016/j.powtec.2021.05.082.

[15] S. Haeri, Optimisation of blade type spreaders for powder bed preparation in additive manufacturing using DEM simulations, Powder Technol. 321 (2017) 94–104, https://doi.org/10.1016/j.powtec.2017.08.011.

[16] D. Schiochet Nasato, H. Briesen, T. Pöschel, Influence of vibrating recoating mechanism for the deposition of powders in additive manufacturing: discrete element simulations of polyamide 12, Addit. Manuf. 48 (2021) 1–11, https://doi.org/10.1016/j.addma.2021.102248.

[17] Z. Snow, R. Martukanitz, S. Joshi, On the development of powder spreadability metrics and feedstock requirements for powder bed fusion additive manufacturing, Addit. Manuf. 28 (2019) 78–86, https://doi.org/10.1016/j.addma.2019.04.017.

[18] A. Mussatto, R. Groarke, A. O'Neill, M.A. Obeidi, Y. Delaure, D. Brabazon, Influences of powder morphology and spreading parameters on the powder bed topography uniformity in powder bed fusion metal additive manufacturing, Addit. Manuf. 38 (2021), 101807, https://doi.org/10.1016/j.addma.2020.101807.

[19] S. Yim, H. Bian, K. Aoyagi, K. Yamanaka, A. Chiba, Spreading behavior of Ti–48Al–2Cr–2Nb powders in powder bed fusion additive manufacturing process: experimental and discrete element method study, Addit. Manuf. 49 (2022), 102489, https://doi.org/10.1016/j.addma.2021.102489.

[20] H. Chen, Q. Wei, S. Wen, Z. Li, Y. Shi, Flow behavior of powder particles in layering process of selective laser melting: numerical modeling and experimental verification based on discrete element method, Int. J. Mach. Tools Manuf. 123 (2017) 146–159, https://doi.org/10.1016/j.ijmachtools.2017.08.004.

[21] E. Gärtner, H.Y. Jung, N.J. Peter, G. Dehm, E.A. Jägle, V. Uhlenwinkel, L. Mädler, Reducing cohesion of metal powders for additive manufacturing by nanoparticle dry-coating, Powder Technol. 379 (2021) 585–595, https://doi.org/10.1016/j.powtec.2020.10.065.

[22] Y.H. Zhou, S.F. Lin, Y.H. Hou, D.W. Wang, P. Zhou, P.L. Han, Y.L. Li, M. Yan, Layered surface structure of gas-atomized high Nb-containing TiAl powder and its impact on laser energy absorption for selective laser melting, Appl. Surf. Sci. 441 (2018) 210–217, https://doi.org/10.1016/j.apsusc.2018.01.296.

[23] Y. Il Kim, D.K. Kim, D. Lee, T.S. Kim, Y. Do Kim, B. Lee, Improving spreadability of hydrogenation–dehydrogenation Ti powder via surface treatment using silane-based compounds, Appl. Surf. Sci. 556 (2021), 149645, https://doi.org/10.1016/j.apsusc.2021.149645.

[24] S. Yim, H. Bian, K. Aoyagi, K. Yanagihara, S. Ichi Kitamura, H. Manabe, Y. Daino, Y. Hayasaka, K. Yamanaka, A. Chiba, Ball-milling treatment of gas-atomized Ti–48Al–2Cr–2Nb powder and its effect on preventing smoking during electron beam powder bed fusion building process, Addit. Manuf. 51 (2022), 102634, https://doi.org/10.1016/j.addma.2022.102634.

[25] A. Chiba, Y. Daino, K. Aoyagi, K. Yamanaka, Smoke suppression in electron beam melting of Inconel 718 alloy powder based on insulator – metal transition of surface, Mater. 14 (2021), https://doi.org/10.3390/ma14164662.

[26] S. Yim, K. Aoyagi, K. Yanagihara, H. Bian, A. Chiba, Effect of mechanical ball milling on the electrical and powder bed properties of gas-atomized Ti–48Al–2Cr–2Nb and elucidation of the smoke mechanism in the powder bed fusion electron beam melting process, J. Mater. Sci. Technol. 137 (2022) 36–55, https://doi.org/10.1016/j.jmst.2022.07.024.

[27] W.-S. Rasband, ImageJ: Image Processing and Analysis in Java, 2012 ascl: 1206.013.

[28] H. Chen, T. Cheng, Z. Li, Q. Wei, W. Yan, Is high-speed powder spreading really unfavourable for the part quality of laser powder bed fusion additive manufacturing? Acta Mater. 231 (2022), 117901 https://doi.org/10.1016/j.actamat.2022.117901.

[29] B. Liu, M. Wang, Y. Du, J. Li, Size-dependent structural properties of a high-Nb TiAl alloy powder, Materials (Basel). 13 (2020) 1–7, https://doi.org/10.3390/ma13010161.

[30] A.I. Gusev, A.S. Kurlov, Production of nanocrystalline powders by high-energy ball milling: model and experiment, Nanotechnology. 19 (2008), https://doi.org/10.1088/0957-4484/19/26/265302.

[31] S. Yim, H. Bian, K. Aoyagi, A. Chiba, Effect of multi-stage heat treatment on mechanical properties and microstructure transformation of Ti–48Al–2Cr–2Nb alloy, Mater. Sci. Eng. A 816 (2021), 141321, https://doi.org/10.1016/j.msea.2021.141321.

[32] M. Habibnejad-korayem, J. Zhang, Y. Zou, Effect of particle size distribution on the flowability of plasma atomized Ti-6Al-4V powders, Powder Technol. 392 (2021) 536–543, https://doi.org/10.1016/j.powtec.2021.07.026.

[33] G. Yablokova, M. Speirs, J. Van Humbeeck, J.P. Kruth, J. Schrooten, R. Cloots, F. Boschini, G. Lumay, J. Luyten, Rheological behavior of β-Ti and NiTi powders produced by atomization for SLM production of open porous orthopedic implants, Powder Technol. 283 (2015) 199–209, https://doi.org/10.1016/j.powtec.2015.05.015.

[34] J.Y.S. Tay, B.W.T. Kok, C.V. Liew, P.W.S. Heng, Effects of particle surface roughness on in-die flow and tableting behavior of lactose, J. Pharm. Sci. 108 (2019) 3011–3019, https://doi.org/10.1016/j.xphs.2019.04.028.

[35] A.B. Spierings, M. Voegtlin, T. Bauer, K. Wegener, Powder flowability characterisation methodology for powder-bed-based metal additive manufacturing, Prog. Addit. Manuf. 1 (2016) 9–20, https://doi.org/10.1007/s40964-015-0001-4.

[36] M.A. Spurek, L. Haferkamp, C. Weiss, A.B. Spierings, J.H. Schleifenbaum, K. Wegener, Influence of the particle size distribution of monomodal 316L powder on its flowability and processability in powder bed fusion, Prog. Addit. Manuf. (2021), https://doi.org/10.1007/s40964-021-00240-z.

[37] I.H. Hwang, B. Jiang, Z. Jin, C.I. Park, S.W. Han, Anomalous structural disorder and distortion in metal-to-insulator-transition Ti2O3, J. Appl. Phys. 119 (2016), https://doi.org/10.1063/1.4939290.

[38] J. Visser, Van der Waals and other cohesive forces affecting powder fluidization, Powder Technol. 58 (1989) 1–10, https://doi.org/10.1016/0032-5910(89)80001-4.

[39] L.J. Jallo, Y. Chen, J. Bowen, F. Etzler, R. Dave, Prediction of inter-particle adhesion force from surface energy and surface roughness, J. Adhes. Sci. Technol. 25 (2011) 367–384, https://doi.org/10.1163/016942410X525623.

[40] M. Leturia, M. Benali, S. Lagarde, I. Ronga, K. Saleh, Characterization of flow properties of cohesive powders: a comparative study of traditional and new testing methods, Powder Technol. 253 (2014) 406–423, https://doi.org/10.1016/j.powtec.2013.11.045.

[41] C. Meier, R. Weissbach, J. Weinberg, W.A. Wall, A., John hart, modeling and characterization of cohesion in fine metal powders with a focus on additive manufacturing process simulations, Powder Technol. 343 (2019) 855–866, https://doi.org/10.1016/j.powtec.2018.11.072.

[42] S. Matsusaka, H. Maruyama, T. Matsuyama, M. Ghadiri, Triboelectric charging of powders: A review, Chem. Eng. Sci. 65 (2010) 5781–5807, https://doi.org/10.1016/j.ces.2010.07.005.

[43] Z.C. Cordero, H.M. Meyer, P. Nandwana, R.R. Dehoff, Powder bed charging during electron-beam additive manufacturing, Acta Mater. 124 (2017) 437–445, https://doi.org/10.1016/j.actamat.2016.11.012.

[44] E. Von Hauff, Impedance spectroscopy for emerging photovoltaics, J. Phys. Chem. C 123 (2019) 11329–11346, https://doi.org/10.1021/acs.jpcc.9b00892.

[45] Y. Zhao, Y. Cui, Y. Hasebe, H. Bian, K. Yamanaka, K. Aoyagi, T. Hagisawa, A. Chiba, Controlling factors determining flowability of powders for additive manufacturing: a combined experimental and simulation study, Powder Technol. 393 (2021) 482–493, https://doi.org/10.1016/j.powtec.2021.08.006.

[46] W. Nan, Y. Gu, Experimental investigation on the spreadability of cohesive and frictional powder, Adv. Powder Technol. 33 (2022), 103466, https://doi.org/10.1016/j.apt.2022.103466.

[47] L. Haferkamp, A. Spierings, M. Rusch, D. Jermann, M.A. Spurek, K. Wegener, Effect of particle size of monomodal 316L powder on powder layer density in powder bed fusion, Prog. Addit. Manuf. (2020), https://doi.org/10.1007/s40964-020-00152-4.

[48] H.H. Zhu, J.Y.H. Fuh, L. Lu, The influence of powder apparent density on the density in direct laser-sintered metallic parts, Int. J. Mach. Tools Manuf. 47 (2007) 294–298, https://doi.org/10.1016/j.ijmachtools.2006.03.019.

[49] H. Chen, Q. Wei, Y. Zhang, F. Chen, Y. Shi, W. Yan, Powder-spreading mechanisms in powder-bed-based additive manufacturing: experiments and computational modeling, Acta Mater. 179 (2019) 158–171, https://doi.org/10.1016/j.actamat.2019.08.030.

[50] C. Pleass, S. Jothi, Influence of powder characteristics and additive manufacturing process parameters on the microstructure and mechanical behaviour of Inconel 625 fabricated by selective laser melting, Addit. Manuf. 24 (2018) 419–431, https://doi.org/10.1016/j.addma.2018.09.023.

[51] Q. Wu, C. Qiao, J. Wang, D. Yao, Y. Wu, W. Fan, M. Li, X. An, Adaptability investigations on bottom modified blade in powder spreading process of additive manufacturing, Addit. Manuf. 49 (2022), 102477, https://doi.org/10.1016/j.addma.2021.102477.